Jungwan Cho[1]
Department of Mechanical Engineering,
Stanford University,
Stanford, CA 94305;
440 Escondido Mall,
Bldg 530/Rm 224,
Stanford, CA 94305-3030
e-mail: jungwan.cho@stanford.edu

Daniel Francis
Element Six Technologies,
Santa Clara, CA 95054
e-mail: daniel.francis@e6.com

Pane C. Chao
Microelectronics Center,
BAE Systems,
Nashua, NH 03060
e-mail: pane.chao@baesystems.com

Mehdi Asheghi
Department of Mechanical Engineering,
Stanford University,
Stanford, CA 94305
e-mail: masheghi@stanford.edu

Kenneth E. Goodson
Fellow ASME
Department of Mechanical Engineering,
Stanford University,
Stanford, CA 94305
e-mail: goodson@stanford.edu

Cross-Plane Phonon Conduction in Polycrystalline Silicon Films

Silicon films of submicrometer thickness play a central role in many advanced technologies for computation and energy conversion. Numerous thermal conductivity data for silicon films are available in the literature, but they are mainly for the lateral, or in-plane, direction for both polycrystalline and single crystalline films. Here, we use time-domain thermoreflectance (TDTR), transmission electron microscopy, and semiclassical phonon transport theory to investigate thermal conduction normal to polycrystalline silicon (polysilicon) films of thickness 79, 176, and 630 nm on a diamond substrate. The data agree with theoretical predictions accounting for the coupled effects of phonon scattering on film boundaries and defects related to grain boundaries. Using the data and the phonon transport model, we extract the normal, or cross-plane thermal conductivity of the polysilicon (11.3 ± 3.5, 14.2 ± 3.5, and 25.6 ± 5.8 W m^{-1} K^{-1} for the 79, 176, and 630 nm films, respectively), as well as the thermal boundary resistance between polysilicon and diamond (6.5–8 m^2 K GW^{-1}) at room temperature. The nonuniformity in the extracted thermal conductivities is due to spatially varying distributions of imperfections in the direction normal to the film associated with nucleation and coalescence of grains and their subsequent columnar growth. [DOI: 10.1115/1.4029820]

Keywords: heat transfer, thermal conductivity, thermal boundary resistance, phonon transport, time-domain thermoreflectance, silicon, polycrystalline films

1 Introduction

While there has been much recent interest in low-dimensional nanostructures based on a variety of novel materials, silicon films remain critical for a large fraction of devices proposed or used for information and energy conversion technologies. Many of these are based on silicon-on-insulator technology, which provides single crystalline silicon films of submicrometer thickness (on top of a buried oxide layer on a bulk silicon substrate) for a large number of applications. These applications include high-performance microprocessors, microfabricated sensors and actuators, and other emerging applications such as phononic crystals [1–3]. Polycrystalline silicon (polysilicon) films have also been used for many applications, including microelectromechanical systems and integrated circuits [4]. Of particular recent interest are polysilicon films on a diamond substrate for heat sink applications in high power electronic devices [5].

Because of the wide use of silicon films in a variety of micro- and nanoscale devices, there have been numerous experimental studies on thermal conduction in both single crystalline and polycrystalline silicon films [2–4,6–17]. Many experimental observations [2,4,6–13] have indicated a large reduction in the thermal conductivities of single crystalline silicon films down to 9 nm thickness [13] due to the strong impact of phonon boundary scattering (for a comprehensive review of the data, see Refs. [2,4]). Other experimental studies of polysilicon films have shown that phonon scattering on grain boundaries significantly decreases the thermal conductivity values compared to those of single crystalline silicon films [14,15]. The thermal conductivity can also be strongly reduced by interactions of phonons with dopants and material defects [14–16,18]. However, the largest quantity of data available in the literature is for lateral, or in-plane, conduction in both single crystalline and polycrystalline films [2,4,6–16]. One study [17] attempted to extract the normal, or cross-plane, thermal conductivity of a 2.6-μm-thick, phosphorus doped polysilicon cantilever; another study [3] extracted this conductivity for 500-nm-thick, suspended, single crystalline silicon films (patterned films with periodic arrays of holes as well as an unpatterned one).

This work investigates thermal conduction normal to polysilicon films with three different thicknesses (79, 176, and 630 nm) on a diamond substrate. We use TDTR and the semiclassical phonon transport theory—which uses an approximate solution to the Boltzmann transport equation (BTE)—to examine effects of phonon scattering by film boundaries and defects related to grain boundaries. Our BTE model considers the nonhomogeneity of the phonon scattering rate internal to the polysilicon film due to the varying grain dimension, and thus to varying distributions of imperfections in the direction normal to the film. By combining the data and the phonon transport model, we extract the cross-plane thermal conductivity of the polysilicon films (11.3 ± 3.5, 14.2 ± 3.5, and 25.6 ± 5.8 W m^{-1} K^{-1} for the 79, 176, and 630 nm films, respectively) and the polysilicon–diamond thermal boundary resistance (6.5–8 m^2 K GW^{-1}) at room temperature.

2 Experimental Details

2.1 Sample Preparation. Three polysilicon films with thicknesses of 79, 176, and 630 nm are grown on a diamond substrate

[1]Corresponding author.
Contributed by the Heat Transfer Division of ASME for publication in the Journal of Heat Transfer. Manuscript received September 10, 2014; final manuscript received February 5, 2015; published online March 24, 2015. Assoc. Editor: Zhuomin Zhang.

Copyright © 2015 by ASME

Downloaded From: http://heattransfer.asmedigitalcollection.asme.org/ on 03/24/2015 Terms of Use: http://asme.org/terms

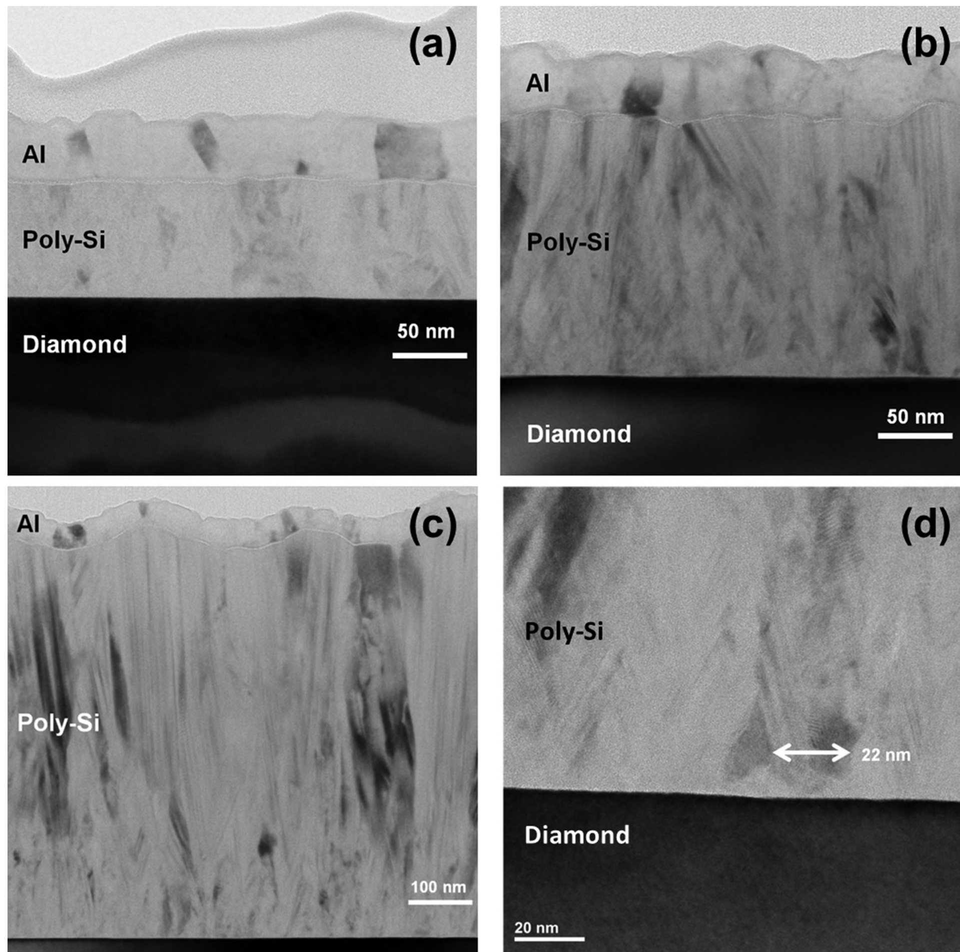

Fig. 1 Cross-sectional TEMs of: (*a*) the 79 nm polysilicon film, (*b*) the 176 nm polysilicon film, and (*c*) the 630 nm polysilicon film on diamond. (*d*) The higher magnification image of the 630 nm sample near the polysilicon–diamond interface shows that the minimum grain dimension of the film at its growth interface (with the diamond) is approximately of the order of a few tens of nanometers. Overall, the micrographs indicate that the grain structure of the polysilicon film becomes columnar with increasing film thickness, and the columnar gains are aligned with respect to the film-normal direction. Approximately 45-nm-thick, evaporated Al films on top of these samples serve as the transducer for thermoreflectance measurements.

by thermal chemical vapor deposition (CVD) at 600 °C. The diamond is a polycrystalline wafer with thermal conductivity on the order of 1500 W m^{-1} K^{-1}. The three polysilicon films are not doped. Figure 1 shows cross-sectional transmission electron micrographs (TEMs) of the three samples, which provide qualitative information about the grain size and orientation in the polysilicon film. With increasing film thickness, the columnar grain structure is clearly visible, with the long axes of the grains oriented in the film-normal direction. This is in agreement with past studies [14,15], which showed that polysilicon films grown by CVD at temperatures between 600 and 650 °C have columnar grain structure. For a film with columnar grains, the lateral grain size increases with increasing distance from the deposition interface of the film [14,15]. An atomic force microscopy (AFM) measurement characterizes the average lateral grain size of a 700-nm-thick polysilicon film that is grown separately but under the same growth conditions as the other three samples. We use the line-intercept method [19] to obtain the average lateral grain size of the 700 nm film from the plan-view AFM image, which yields 360 ± 80 nm. The higher magnification TEM of the 630 nm film near the polysilicon–diamond interface shows that the minimum grain dimension of the film at its growth interface is approximately of the order of a few ten nanometers (see Fig. 1(*d*)). We determine the minimum grain dimension more precisely by comparing our BTE model with TDTR data later in Sec. 3. We evaporate approximately 45-nm-thick Al—which serves as the transducer for thermoreflectance measurements—on the surface of the three polysilicon films after an extended air break.

2.2 TDTR. Cross-plane thermal conduction from the polysilicon to the diamond substrate is investigated by TDTR, an ultrafast optical measurement technique using a pump–probe arrangement. This technique is well-established for measuring cross-plane thermal conductivity and thermal boundary resistance in multilayer thin-film structures [20–27]. In our setup, a mode-locked $Nd{:}YVO_4$ laser emits 9.2 ps optical pulses at a wavelength of 1064 nm and a repetition rate of 82 MHz, which are divided into a pump (as a heater) and probe (as a thermometer) component. Pump pulses are modulated at a frequency of 2 MHz using an electro-optic modulator for lock-in detection and are frequency-doubled to 532 nm using a periodically poled $LiNbO_3$ crystal for the spectral separation of the pump and probe pulses. The modulated pump pulses rapidly heat the metal transducer and create a transient temperature field within the material stack. The probe pulses are temporally delayed (from 0 to 3.5 ns) with respect to the pump optical heating by using a mechanical delay stage, and they measure the transient surface temperature decay of the metal

Downloaded From: http://heattransfer.asmedigitalcollection.asme.org/ on 03/24/2015 Terms of Use: http://asme.org/terms

film via the temperature-induced changes in the metal reflectivity. The changes in the reflected intensity of the probe pulses are detected by an RF lock-in amplifier at the modulation frequency of the pump pulses as a function of the delay time t between the pump and probe pulses. The $1/e^2$ diameters of the focused pump and probe beams are $\sim$10 and $\sim$6 μm, respectively, in our experiments.

We monitor the amplitude $\sqrt{V_{\text{in}}^2 + V_{\text{out}}^2}$ of the in-phase $V_{\text{in}}(t)$ and out-of-phase $V_{\text{out}}(t)$ voltage signals of the RF lock-in amplifier over 3.5 ns of delay time between pump and probe. We use a single-mode fiber after the delay stage to address the problems created by (i) changes in the probe spot size and (ii) variations in the alignment and overlap of the pump and probe beams as the delay time is varied [20,25,26]. The pump beam amplitude and the delay-time-dependent amplitude of the probe beam are monitored independently from the thermoreflectance amplitude signal to correct for intensity fluctuations and for the intensity dependence on the stage position [25,26]. The corrected thermoreflectance amplitude data are fitted to the solution of the three-dimensional radial-symmetric heat diffusion equation for the multilayer stack taking into account surface heating by a modulated periodic pulse train to extract the relevant thermal properties beneath the metal transducer [21]. We validate system accuracy by extracting a room-temperature thermal conductivity of 1.33 ± 0.1 W m^{-1} K^{-1} and 145 ± 15 W m^{-1} K^{-1} for a SiO_2 calibration sample and an intrinsic single crystalline Si calibration sample, respectively, each of which is within 2% of reference literature values for thermally grown SiO_2 and bulk single crystalline silicon [28,29]. Further details of our TDTR setup are described in Refs. [25,26].

We fit the TDTR data with three adjustable parameters in the analytical heat diffusion model: (i) the thermal boundary resistance at the Al–polysilicon interface $R_{\text{b,Al–Si}}$, (ii) the cross-plane thermal conductivity of the polysilicon film k_{Si}, and (iii) the thermal boundary resistance at the polysilicon–diamond interface $R_{\text{b,Si–Diam}}$. The validity of this approach is addressed through a discussion of sensitivity in Sec. 2.3. All the other parameters in the multilayer thermal model are taken from the literature or measured independently. We use literature values for the volumetric heat capacities of the constituent layers (i.e., Al, polysilicon, and diamond) [30–32]. Cross-sectional TEMs shown in Fig. 1 confirm the layer thicknesses. The thermal conductivity of the Al transducer film is estimated from the in-plane electrical conductivity of the Al film and the use of the Wiedemann–Franz–Lorenz law. The thermal conductivity of the diamond substrate is assumed to have a value of 1500 W m^{-1} K^{-1}, taken from manufacturer's specification (>1500 W m^{-1} K^{-1} at room temperature), corresponding to the conductivity values for high-quality polycrystalline CVD diamond [32–34]. As we discuss in Sec. 2.3, sensitivity analysis shows that a small variation in the diamond thermal conductivity has a negligible impact on the fitted variables.

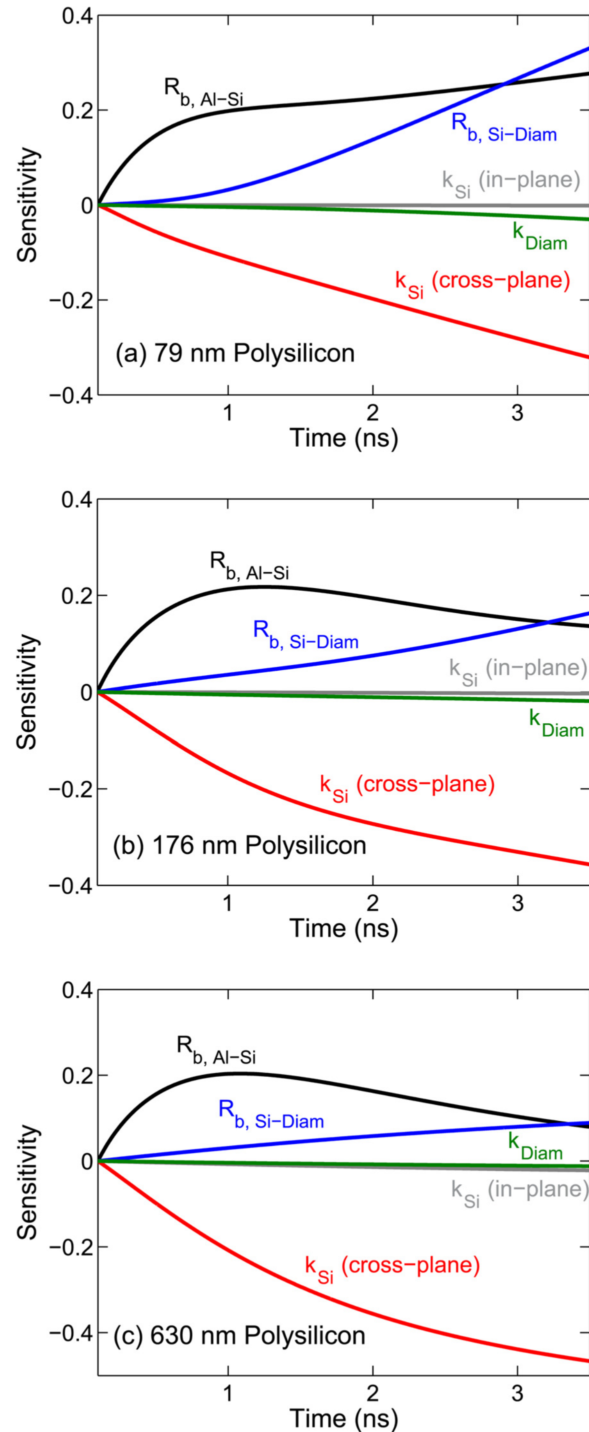

Fig. 2 Sensitivity of the TDTR amplitude signal, calculated via Eq. (1), for the three polysilicon samples to the thermal boundary resistance between the Al and polysilicon $R_{\text{b,Al–Si}}$, the cross-plane thermal conductivity of the polysilicon film k_{Si} (cross-plane), the in-plane thermal conductivity of the polysilicon film k_{Si} (in-plane), the thermal boundary resistance between the polysilicon and diamond $R_{\text{b,Si–Diam}}$, and the thermal conductivity of the diamond substrate k_{Diam}. The values of the sensitivity coefficients are evaluated at a pump modulation frequency of 2 MHz and as a function of the pump–probe delay time. The thickness of the polysilicon film is 79 nm in (*a*), 176 nm in (*b*), and 630 nm in (*c*).

2.3 Sensitivity Analysis. The TDTR sensitivity coefficient is defined as the logarithmic derivative of the thermoreflectance signal R with respect to the thermal parameter of interest β [23,24,26,27]

$$S_\beta = \frac{\partial \ln(R)}{\partial \ln(\beta)} \qquad (1)$$

For the TDTR measurements in the present study, R is the amplitude signal $\sqrt{V_{\text{in}}^2 + V_{\text{out}}^2}$. (We discuss in more detail the TDTR signal approach later in this section.) Figure 2 shows the sensitivity of the amplitude signal to the three unknown parameters (i.e., $R_{\text{b,Al–Si}}$, k_{Si}, and $R_{\text{b,Si–Diam}}$) and to the thermal conductivity of the diamond substrate k_{Diam} as a function of the delay time for the three polysilicon samples at room temperature. The values of the sensitivity coefficients are evaluated at the 2 MHz pump modulation frequency and assuming best-fit values for each of the fitted variables. For all three samples, the sensitivity of the amplitude signal to $R_{\text{b,Al–Si}}$ is different from that to k_{Si} and $R_{\text{b,Si–Diam}}$ in terms of the curvature. Since the sensitivity to $R_{\text{b,Al–Si}}$ is highly

Downloaded From: http://heattransfer.asmedigitalcollection.asme.org/ on 03/24/2015 Terms of Use: http://asme.org/terms

dependent on the earliest part of the thermoreflectance traces (at delay times below approximately 1 ns), its values increase with increasing delay time up to ∼1 ns, whereas at longer delay times ($t > 1$ ns) they remain relatively constant (see Fig. 2(*a*)) or decrease with delay time (see Figs. 2(*b*) and 2(*c*)). On the other hand, the absolute values of the sensitivity to k_{Si} and $R_{b,Si-Diam}$ monotonically increase with increasing delay time. These different curvatures of the sensitivities allow us to separate the Al–polysilicon boundary resistance from the other two components (k_{Si} and $R_{b,Si-Diam}$). The latter two are not possible to uniquely separate since their sensitivity curves are similar in shape over the entire range of delay time. They are rather lumped into an effective polysilicon thermal resistance $R_{Si,eff}$ that combines the volumetric polysilicon resistance d_{Si}/k_{Si}(where d_{Si} is the thickness of the polysilicon film) and the polysilicon–diamond boundary resistance [27,35–37], which can be expressed as

$$R_{Si,eff} = \frac{d_{Si}}{k_{Si}} + R_{b,Si-Diam} \quad (2)$$

The measurement is insensitive to the in-plane heat conduction along the polysilicon films because the sensitivity to the in-plane polysilicon thermal conductivity is essentially zero for all three samples (as illustrated in Fig. 2). The sensitivity to k_{Diam} is also extremely low for all three samples. The absolute sensitivity values are ∼0.03 and ∼0.01 for the thinnest and thickest polysilicon samples, respectively. Therefore, variations in the diamond thermal conductivity will not significantly impact the fitted variables—e.g., a 30% error in the diamond thermal conductivity propagates to a 2% error in the effective polysilicon thermal resistance for the thinnest sample and a 1% error for the thickest sample.

To further support the validity of our data fitting approach, we plot the TDTR data along with the optimal analytical fit for the 176 nm polysilicon sample in Fig. 3(*a*), and we also illustrate degenerate solutions by varying $R_{b,Si-Diam}$ from its optimal value (±10%) and then reoptimizing the remaining two free parameters ($R_{b,Al-Si}$ and k_{Si}). The reoptimized polysilicon thermal conductivity varies by −4.1% from its original optimal value due to the −10% perturbation in $R_{b,Si-Diam}$ (see dashed–dotted line in Fig. 3(*a*)); this variation in the polysilicon thermal conductivity is +4.5% for the +10% perturbation in $R_{b,Si-Diam}$ (see dotted line in Fig. 3(*a*)). The variations in $R_{b,Al-Si}$ due to the ±10% perturbation in $R_{b,Si-Diam}$ are negligible. Since these three analytical fits, with different combinations of k_{Si} and $R_{b,Si-Diam}$, are not distinguishable from each other and replicate the data well, this indicates that the TDTR measurement is not able to uniquely separate k_{Si} and $R_{b,Si-Diam}$. Instead, the measurement is sensitive to the sum of the polysilicon volume resistance and the polysilicon–diamond boundary resistance (i.e., sensitive to the effective polysilicon thermal resistance $R_{Si,eff}$, as suggested above). Figure 3(*b*) presents the TDTR data and the optimal analytical fit for the thinnest sample (79 nm) and also illustrates the sensitivity of the TDTR measurement to k_{Diam} for this sample—where the diamond thermal conductivity is expected to play the largest role. This analysis clearly shows that variations in the diamond thermal conductivity (e.g., ±30%) have a negligible impact on the thermal trace of the samples.

In typical TDTR experiments, both the amplitude $\sqrt{V_{in}^2 + V_{out}^2}$ and the ratio $-V_{in}/V_{out}$ of the in-phase and out-of-phase voltage signals of the RF lock-in amplifier versus delay time can be analyzed to extract the relevant thermal properties (e.g., the sample thermal conductivity). We have found that both the amplitude and ratio approaches offer sufficient sensitivity to extract the thermal conductivity of samples having low to intermediate conductivity values—from that of thermally grown SiO_2 (∼1.4 W m^{-1} K^{-1}) to that of bulk single crystalline silicon (∼150 W m^{-1} K^{-1}) [26,27,38]. However, if the sample thermal conductivity is higher than this range of values, the ratio approach provides higher sensitivity to extract the sample conductivity than the amplitude approach [27,38].

The cross-plane thermal conductivity values of our three polysilicon films range from approximately 11 to 26 W m^{-1} K^{-1} (we present these results in more detail in Sec. 3), and they hence are approximately an order of magnitude lower than that of bulk single crystalline silicon. This means that both the amplitude and ratio approaches can be used for our polysilicon samples. We choose to analyze the amplitude signal in this study because the amplitude approach has some advantages over the ratio approach-for this specific set of samples:

(1) The error propagated by the uncertainty in the thermal conductivity of the diamond substrate k_{Diam} is smaller in the

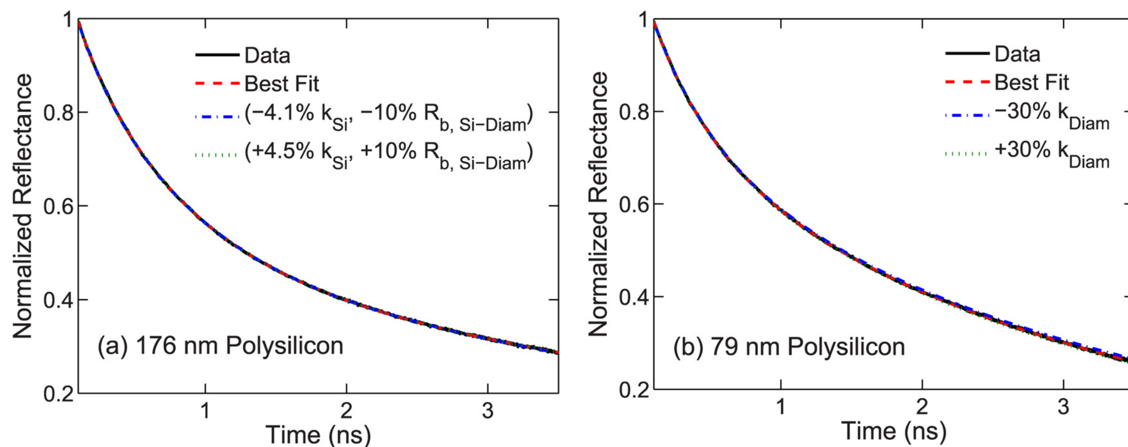

Fig. 3 (*a*) TDTR data for the 176 nm polysilicon sample (solid line) along with the best analytical fit (dashed line) yielding the optimal parameter set $R_{b,Al-Si}$ = 6.7 m^2 K GW^{-1}, k_{Si} = 14.7 W m^{-1} K^{-1}, and $R_{b,Si-Diam}$ = 7.7 m^2 K GW^{-1}. The dashed–dotted and dotted curves represent the analytical fits obtained by varying best-fit $R_{b,Si-Diam}$ by −10% and +10%, respectively, and then by reoptimizing $R_{b,Al-Si}$ and k_{Si}. The re-optimized polysilicon thermal conductivity varies by −4.1% (dashed–dotted line) and +4.5% (dotted line) from its original optimal value of 14.7 W m^{-1} K^{-1}. The variations in $R_{b,Al-Si}$ are negligible. (*b*) TDTR data for the 79 nm polysilicon sample (solid line) along with the best analytical fit (dashed line) yielding the optimal parameter set $R_{b,Al-Si}$ = 7.5 m^2 K GW^{-1}, k_{Si} = 12.0 m^2 K GW^{-1}, and $R_{b,Si-Diam}$ = 6.8 m^2 K GW^{-1}. The best-fit curve assumes k_{Diam} = 1500 W m^{-1} K^{-1} (from manufacturer's specification). The dashed–dotted and dotted curves represent the analytical fits obtained by varying this diamond thermal conductivity by −30% and +30%, respectively, and by assuming best-fit values for each of the fitted variables.

Downloaded From: http://heattransfer.asmedigitalcollection.asme.org/ on 03/24/2015 Terms of Use: http://asme.org/terms

amplitude approach than in the ratio approach because the latter is more sensitive to the diamond substrate thermal conductivity than the former [26]. The propagation of uncertainty from k_{Diam} into the uncertainties of the measured properties (k_{Si} and $R_{\mathrm{b,Si-Diam}}$) is proportional to the ratio of the sensitivities to these properties, i.e., $S_{k_{\mathrm{Diam}}}/S_{k_{\mathrm{Si}}}$ and $S_{k_{\mathrm{Diam}}}/S_{R_{\mathrm{b}},\mathrm{Si-Diam}}$. (The error propagation is this ratio—$S_{k_{\mathrm{Diam}}}/S_{k_{\mathrm{Si}}}$ or $S_{k_{\mathrm{Diam}}}/S_{R_{\mathrm{b}},\mathrm{Si-Diam}}$—multiplied by the uncertainty in k_{Diam}.) The absolute values of these two ratios for the thinnest sample (79 nm) are $|S_{k_{\mathrm{Diam}}}/S_{k_{\mathrm{Si}}}| < 0.2$ and $|S_{k_{\mathrm{Diam}}}/S_{R_{\mathrm{b}},\mathrm{Si-Diam}}| < 0.6$ for the amplitude approach and $|S_{k_{\mathrm{Diam}}}/S_{k_{\mathrm{Si}}}| > 2$ and $|S_{k_{\mathrm{Diam}}}/S_{R_{\mathrm{b}},\mathrm{Si-Diam}}| > 1.3$ for the ratio approach—all at delay times from 100 ps to 3.5 ns. For the thickest sample (630 nm), $|S_{k_{\mathrm{Diam}}}/S_{k_{\mathrm{Si}}}| < 0.05$ and $|S_{k_{\mathrm{Diam}}}/S_{R_{\mathrm{b}},\mathrm{Si-Diam}}| < 0.23$ for the amplitude approach and $|S_{k_{\mathrm{Diam}}}/S_{k_{\mathrm{Si}}}| > 0.16$ and $|S_{k_{\mathrm{Diam}}}/S_{R_{\mathrm{b}},\mathrm{Si-Diam}}| > 0.38$ for the ratio approach—all at delay times from 100 ps to 3.5 ns.

(2) The amplitude approach is free of error propagation associated withthe uncertainty in setting the correct reference phase of the RFlock-in amplifier, whereas in the ratio approach thisuncertainty is one of the major sources of the total uncertainty, especially for a low-frequency measurement [24]. Since we use a relatively low pump modulation frequency of 2MHz to probe the buried film–substrate interface, the amplitude approach is beneficial for extracting the thermal resistance of this buried interface with lower uncertainty [26].

The thermal penetration depths of the modulated pump beam at 2 MHz correspond to approximately 1–1.6 μm polysilicon (depending on the polysilicon thermal conductivity), which are larger than the three polysilicon thicknesses. The 2 MHz data are thus sensitive to both the polysilicon conductivity and the polysilicon–diamond boundary resistance, as illustrated in Fig. 2. The thermal penetration depths at higher modulation frequencies are smaller than those at 2 MHz; e.g., the thermal penetration depths at 5 MHz and 8 MHz correspond to approximately 0.7–1 μm and 0.5–0.8 μm polysilicon, respectively. TDTR measurements are also performed on each sample at 5 MHz, at which the thermal penetration depths are still larger than the film thicknesses. No modulation frequency dependence is observed between the 2 MHz and 5 MHz data; variations in the extracted parametersare less than 3%.

3 Results and Discussion

A nonlinear least-squares curve-fitting algorithm finds the Al–polysilicon thermal boundary resistance and the effective polysilicon thermal resistance that optimize the model fit to the measured TDTR data. We normalize the TDTR data at 100 ps to minimize the influence of nonequilibrium phenomena (e.g., electron–phonon coupling effects in the Al transducer film within the first tens of picoseconds after the pump heating) on our data fitting results, and we fit the data over the range of delay time, 100 ps $< t <$ 3.5 ns. Changing the normalization time by 50% results in a less than 2% change in the data fitting results. We find the effective polysilicon thermal resistance to be 13.4 ± 1.8 m^2 K GW^{-1} for the 79 nm sample, 19.7 ± 2.4 m^2 K GW^{-1} for the 176 nm sample, and 32.7 ± 4.5 m^2 K GW^{-1} for the 630 nm sample—all at room temperature. The Al–polysilicon boundary resistances are determined to be 7.5 ± 0.4 m^2 K GW^{-1} for the 79 nm sample, 6.7 ± 0.5 m^2 K GW^{-1} for the 176 nm sample, and 6.0 ± 1.0 m^2 K GW^{-1} for the 630 nm sample—all at room temperature. Our measured Al–polysilicon boundary resistances agree well with previous reports in the literature of the thermal boundary resistance across an Al/native oxide/single crystal Si interface (4–11 m^2 K GW^{-1} [3,39–43]). This variation in the literature values can be attributed to (i) varying concentrations of crystalline imperfections around the interface [39], (ii) impurities and contamination effects [40], (iii) effects of different surface roughnesses [39,41,42], and (iv) effects of different thicknesses of native oxide [39,42]. Note that literature values for an Al–Si interface with the native oxide removed are relatively lower, i.e., 3–6 m^2 K GW^{-1} [39,43,44]. Uncertainties in the thickness of the Al film transducer (46 ± 6 nm for the thickest sample and 44 ± 4 nm for the other two, thinner, samples) govern the extent of the error bars for our fitted parameters [24,26,27,45]. Variations in the other fixed thermal parameters do not significantly impact the fitted parameters (see Sec. 2.3).

The rate of increase in the effective resistance of the polysilicon film and its interface with the diamond decays rapidly with increasing film thickness. That is, a factor of 8 increase in the film thickness from 79 to 630 nm results in a 2.4 times increase in the effective resistance from 13.4 to 32.7 m^2 K GW^{-1}, while a factor of 2 increase in the film thickness from 79 to 176 nm results in a 1.5 times increase in the effective resistance from 13.4 to 19.7 m^2 K GW^{-1}. This indicates that a highly imperfect and small-grained region exists near the polysilicon–diamond interface [46–48], which substantially impairs phonon conduction from the polysilicon film into the diamond substrate. The existence of the near-interfacial, small-grained region, as well as the dependence of grain size on the distance from the growth interface, implies that the local, cross-plane polysilicon thermal conductivity is nonuniform within the film.

We perform simulations of the thermal resistance for conduction normal to the polysilicon film, which account for acoustic mismatch at the two interfaces of the polysilicon (with the Al and with the diamond) and potential sources of phonon scattering within the volume of the polysilicon. In this simulation, we extend the standard version of the semiclassical phonon conductivity integral for Si [49] to account for the combined effects of boundary and grain boundary scattering in polycrystalline thin films [46,48]. An approximate solution to the phonon BTE for conduction normal to a nonhomogeneous film can be written as

$$\frac{1}{R_{\mathrm{T}}} = \frac{1}{3v_s} \sum_{j=\mathrm{L,TO,TU}} v_j^2 \int_0^{\theta_j/T} \frac{C_{V,j}(x_\omega, T)}{d_{E,j}(x_\omega, T) + \frac{4}{3}\left(\frac{1}{\alpha_0} + \frac{1}{\alpha_1} - 1\right)} dx_\omega \tag{3}$$

where the subscript j refers to the longitudinal phonon (L) and the low and high frequency transverse phonon (TO and TU) modes, v_j is the appropriate phonon group velocity for the different modes, v_s is the averaged phonon group velocity, θ_j is the Debye temperature, and $x_\omega = \hbar\omega/k_B T$ is the dimensionless phonon frequency. The phonon specific-heat function $C_V, j(x_\omega, T)$ can be found in Ref. [14]. The diffuse mismatch model (DMM) [50,51] is employed to predict the rates of phonon transmission from within the polysilicon into the Al and the diamond, which are α_0 and α_1, respectively (see Table 1). This form of the BTE model has yielded predictions that were consistent with experimental data when a crystalline dielectric or semiconductor layer—with thickness comparable to mean free paths of phonons—is sandwiched between two media [26,48,52–54].

To consider the nonhomogeneity of the internal phonon scattering rate in the polysilicon film due to the varying grain

Table 1 BTE model parameters. (The normal and Umklapp scattering parameters as well as the detailed phonon properties of Si (such as the phonon group velocities and the Debye temperatures) are taken directly from Ref. [49]).

α_0 [a]	α_1 [a]	d_{G0} (nm)	$n_{\mathrm{GB,P}}$ ($\times 10^{19}\ m^{-2}$)
0.74	0.16	50	1.5

[a]The transmission coefficients determined by the DMM [50] for the phonon transmission from the polysilicon into the Al (α_0) and the diamond (α_1).

Downloaded From: http://heattransfer.asmedigitalcollection.asme.org/ on 03/24/2015 Terms of Use: http://asme.org/terms

dimensions, we define the dimensionless layer thickness as [46,48]

$$d_{E,j}(x_\omega, T) = \int_0^{d_{\rm Si}} \frac{dz}{v_s \tau_j(z, x_\omega, T)} \tag{4}$$

where z is the coordinate normal to the polysilicon film, measured from the polysilicon–diamond interface. The total internal phonon scattering rate τ_j^{-1} of each of the phonon modes (i.e., longitudinal and low/high frequency transverse modes) is the sum of the phonon–phonon (normal or Umklapp) and the grain boundary scattering rates (according to Matthiessen's rule). The normal and Umklapp scattering parameters as well as the detailed phonon properties of Si (such as the phonon group velocities and the Debye temperatures) are taken directly from Ref. [49]. We use the grain boundary scattering term $\tau_{\rm GB}(z, x_\omega)^{-1}$ that was developed in prior studies [46,48] for polycrystalline diamond thin films with columnar grains. These past studies revealed that for the polycrystalline films phonon scattering on localized defects concentrated near grain boundaries may be more important than scattering on grain boundaries and on defects homogeneously distributed within grains. Even if defects homogeneously distributed within grains are important, Eqs. (3) and (4) can be used together with this hypothesis to study the impact of spatial variations of imperfections under the assumption that their concentrations correlate inversely with the grain size.

The BTE model (Eq. (3)) considers two grain structures of polycrystalline films: (i) randomly oriented grains and (ii) entirely columnar grains (with respect to the film-normal direction). Practical, CVD-grown polycrystalline films have grain structures between these two extremes due to the process of nucleation and coalescence of grains during the initial growth stage and the subsequent columnar growth of grains normal to the growth interface. For both grain structures, defects related to grain boundaries are assumed to be concentrated very near grain boundaries [46,48]. The phonon scattering rate due to defects concentrated near grain boundaries is given by

$$\tau_{\rm GB}(z, x_\omega)^{-1} = \frac{2 v_s \eta(z, x_\omega)}{d_{\rm G}(z)} \tag{5}$$

for the case of a random grain structure, and it is given by

$$\tau_{\rm GB}(z, x_\omega)^{-1} = \frac{2 v_s}{\pi d_{\rm G}(z)} \left(1 + \frac{1}{\exp[(\pi/2)^2 \eta(z, x_\omega)] - 1}\right)^{-1} \tag{6}$$

for the case of a perfect columnar grain structure [46,48]. Here, $d_{\rm G}(z)$ is the characteristic grain dimension, i.e., the average lateral grain size, and $\eta(z, x_\omega)$ is the dimensionless grain boundary scattering strength. The latter is defined as [46,48]

$$\eta(z, x_\omega) = \sum_i \sigma_i(x_\omega) n_{{\rm GB},i}(z) \tag{7}$$

where σ_i is the scattering cross section of defects of type i, and $n_{{\rm GB},i}$ is the number density of those defects per unit grain boundary area. This scattering strength of grain boundaries η is assumed here not to vary significantly within a given film [46,48], in other words, $n_{{\rm GB},i}$ is assumed to be constant throughout the thickness of the film. The concentrations of defects per unit volume therefore vary inversely with the grain size: the nucleation/coalescence region of the film (near the growth interface) has smaller average grain size and accordingly higher concentration of grain boundaries, and therefore it has higher defect concentrations than the regions away from the growth interface. In this simple first model, we consider only phonon scattering on point defects for simplicity. (Future modeling could become more refined—albeit at the expense of introducing the ambiguity created by additional adjustable parameters—by considering scattering on dislocations, stacking faults, and even phase impurities [55].) With this restriction, Eq. (7) can be simplified to

$$\eta(x_\omega) = \frac{V_0^2 x_\omega^4 T^4}{4\pi v_s^4} \left(\frac{k_{\rm B}}{\hbar}\right)^4 n_{\rm GB,P} \tag{8}$$

where V_0 is the unit volume for each atom, $\hbar$ is Plank's constant divided by 2π, $k_{\rm B}$ is the Boltzmann constant, and $n_{\rm GB,P}$ is the number density of point defects per unit grain boundary area. The characteristic grain dimension $d_{\rm G}(z)$ is assumed to increase linearly with increasing z [14,15,46,48], with the average lateral grain size of 360 nm for the separately grown 700-nm-thick film (as discussed in Sec. 2.1).

These procedures leave two unknown parameters in the BTE model: (i) the minimum grain dimension at the growth interface $d_{\rm G0} = d_{\rm G}(z = 0)$ and (ii) the number density of point defects per unit grain boundary area $n_{\rm GB,P}$. The two past studies for polysilicon films estimated that the minimum grain size $d_{\rm G0}$ is of the order of 100 nm for doped films [14] and of 10 nm for an undoped film [15]. The former, relatively large minimum grain size of the doped polysilicon films could be attributed to the high temperature annealing process—which promotes grain growth—performed in this specific past study [14] at temperatures around 1100 °C. The minimum grain dimension for our undoped polysilicon films is therefore expected to be close to 10 nm. This is consistent with the observation made in the higher magnification micrograph (see Fig. 1(*d*)), which shows that the minimum grain dimension is roughly of the order of a few tens of nanometers. We determine the two unknown parameters ($d_{\rm G0}$ and $n_{\rm GB,P}$) by comparing with the TDTR data.

Figure 4 shows the total thermal resistance for conduction normal to the polysilicon films as a function of film thickness along with the predictions of the BTE model. The total thermal resistance $R_{\rm T}$ is defined as the sum of the volume resistance of the polysilicon film and the two boundary resistances at its interfaces (with the Al and the diamond) and can be expressed as

$$\begin{aligned} R_{\rm T} &= R_{\rm b,Al-Si} + R_{\rm Si,eff} \\ &= R_{\rm b,Al-Si} + \frac{d_{\rm Si}}{k_{\rm Si}} + R_{\rm b,Si-Diam} \end{aligned} \tag{9}$$

The BTE model compares two grain structures as discussed above: a random grain structure and a perfect columnar grain structure. The latter structure results in less phonon scattering by grain boundaries and related defects and thus lower thermal resistance for conduction normal to the film than the former structure. Figure 4(*a*) shows the effect of variations in $d_{\rm G0}$ on the total thermal resistance assuming $n_{\rm GB,P} = 1.5 \times 10^{19}\,{\rm m}^{-2}$. The data for the 79 and 176 nm samples agree well with the prediction when we assume the grain structure to be random, with $d_{\rm G0} = 50$ nm and $n_{\rm GB,P} = 1.5 \times 10^{19}\,{\rm m}^{-2}$ (see an upper solid line in Fig. 4(*a*)). Since the initial film growth incorporates a highly defective, small-grained region associated with nucleation and grain coalescence, the random grain structure model well describes the data for the two samples. The data for the thickest sample (630 nm) are slightly overpredicted by the random grain structure model and underpredicted by the columnar grain structure model, due to the transition from random to columnar grain structure with increasing film thickness as demonstrated in Fig. 1. Figure 4(*b*) illustrates the effect of varying $n_{\rm GB,P}$—from 1.5×10^{19} to $3.0 \times 10^{19}\,{\rm m}^{-2}$—on the total thermal resistance assuming $d_{\rm G0} = 50$ nm. The effect of increasing $n_{\rm GB,P}$ is more clearly visible in the random grain structure model than in the columnar grain structure model. The model predictions are extrapolated to zero film thickness to determine the summed boundary resistance due to the two polysilicon interfaces ($R_{\rm b,Al-Si} + R_{\rm b,Si-Diam}$) according to Eq. (9). As indicated in Figs. 4(*a*) and 4(*b*), this summed boundary resistance due to the

Downloaded From: http://heattransfer.asmedigitalcollection.asme.org/ on 03/24/2015 Terms of Use: http://asme.org/terms

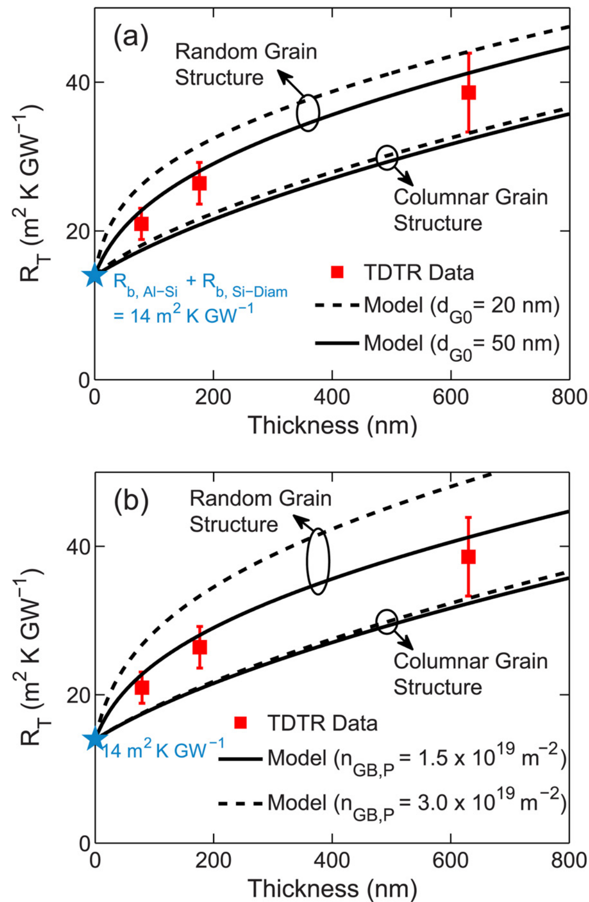

Fig. 4 Total summed thermal resistance R_T for conduction normal to the polysilicon films as a function of film thickness, including the volume resistance of the polysilicon and the boundary resistances at its interfaces (with the Al and with the diamond), along with the predictions of the BTE model (Eq. (3)). (*a*) The BTE model considers the minimum grain dimensions d_{G0} of 20 and 50 nm for the two cases of randomly oriented grains and entirely columnar grains. The number density of point defects per unit grain boundary area $n_{GB,P}$ is assumed to be $1.5 \times 10^{19}\,m^{-2}$. (*b*) The point defect density $n_{GB,P}$ is varied from 1.5×10^{19} to $3.0 \times 10^{19}\,m^{-2}$ while assuming $d_{G0} = 50$ nm.

two interfaces is approximately 14 m^2 K GW^{-1}. Since the measured Al–polysilicon boundary resistance ranges between 6 and 7.5 m^2 K GW^{-1} for the three samples, the polysilicon–diamond boundary resistance is estimated to be 6.5–8 m^2 K GW^{-1}.

The cross-plane polysilicon thermal conductivity data are obtained for all three measured samples by subtracting the sum of the two boundary resistances (i.e., 14 m^2 K GW^{-1}) from the total thermal resistance. This procedure yields the thermal conductivity of 11.3 ± 3.5 W m^{-1} K^{-1} for the 79 nm sample, 14.2 ± 3.5 W m^{-1} K^{-1} for the 176 nm sample, and 25.6 ± 5.8 W m^{-1} K^{-1} for the 630 nm sample. These conductivity values agree with those determined by assuming the above specified range of values for the polysilicon–diamond boundary resistance (i.e., 6.5–8 m^2 K GW^{-1}) and by fitting for the polysilicon thermal conductivity for all three measured samples. It is worth noting that each conductivity value determined here is an average over the entire film thickness, and that spatially varying imperfections along the film-normal direction (and thus the spatially varying phonon scattering rate along this direction) create the nonuniformity in the conductivity values.

Figure 5 shows the room-temperature cross-plane and in-plane thermal conductivity data of silicon films, including our cross-plane polysilicon data and other data available in the literature.

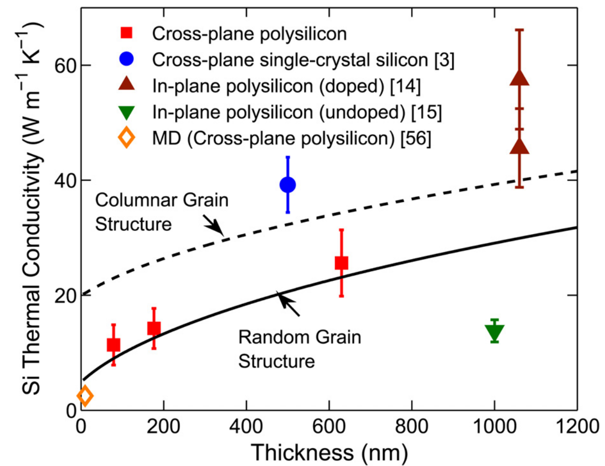

Fig. 5 Room-temperature thermal conductivity of silicon films as a function of film thickness. The cross-plane thermal conductivity data for our three polysilicon films and a suspended 500-nm-thick single crystalline silicon film [3] are depicted by the filled squares and the filled circle, respectively. The in-plane thermal conductivity data for doped polysilicon films [14] and an undoped polysilicon film [15] are depicted by the up-facing and down-facing filled triangles, respectively. The MD calculation for the cross-plane thermal conductivity of a 10-nm-thick polysilicon film [56] (unfiled diamond) is shown for comparison. This MD calculation assumes a random shape of grains and an average grain size of 4 nm. The results of the BTE model for the cross-plane polysilicon thermal conductivity from Eq. (3) (with the boundary resistances removed) are shown with the solid (random grain structure) and dashed (columnar grain structure) lines.

Also shown are the predictions of the BTE model for the cross-plane polysilicon thermal conductivity from Eq. (3) (with the boundary resistances removed), which consider both random and columnar grain structures and assume $d_{G0} = 50$ nm and $n_{GB,P} = 1.5 \times 10^{19}\,m^{-2}$. The cross-plane thermal conductivity values for our three polysilicon films are lower than that of a suspended 500-nm-thick single crystalline silicon film [3] (measured by TDTR) due to the impact of phonon scattering on grain boundaries and related defects. Steady-state Joule heating and electrical-resistance thermometry were used to measure the in-plane thermal conductivity of doped polysilicon films [14] and an undoped polysilicon film [15], all of which were approximately 1-μm-thick and suspended. The in-plane thermal conductivity values of the doped polysilicon films [14] are higher than our conductivity values. This could be attributed to the effects of the high temperature annealing process performed in these doped films, which caused the larger grain dimensions (the maximum grain dimension of approximately 400 nm and the minimum grain dimension of 100 nm) [14], and likely caused fewer defects. The in-plane thermal conductivity of the undoped polysilicon film [15] is lower than our measured conductivity, which could be partly attributed to the smaller grain dimensions of this undoped film (the maximum grain dimension of 210 nm and the minimum grain dimension of 10 nm) [15] and to the conductivity anisotropy observed in polycrystalline materials with columnar grains [32–34,38,48].

As indicated in Fig. 5, the cross-plane thermal conductivity data for the 79 and 176 nm films again agree well with the prediction of the random grain structure model (see a solid line). The data for the thickest film (630 nm) are slightly above the prediction of the random grain structure model, which indicates the transition from random to columnar grain structure with increasing film thickness (as discussed above). Figure 5 also includes the molecular dynamics (MD) calculation for the cross-plane thermal

Downloaded From: http://heattransfer.asmedigitalcollection.asme.org/ on 03/24/2015 Terms of Use: http://asme.org/terms

conductivity of a 10-nm-thick polysilicon film with a random shape of grains and an average grain size of 4 nm [56]. This MD calculation is consistent with the predictions of our BTE model.

We make a further effort here to extract the local, cross-plane polysilicon thermal conductivity $k_{\mathrm{Si,local}}(z)$—which depends on the distance z from the growth interface—by utilizing our three different thickness samples, which share the same microstructure. As a first step, we use the data for the 79 and 176 nm samples and determine the local thermal conductivity corresponding to a region of 79 nm $< z <$ 176 nm. Assuming that we know the volume resistance of the polysilicon corresponding to a region of 0 nm $< z <$ 79 nm, and the bottom boundary resistance (the sum of the two is the effective resistance of the 79 nm film, as we determined earlier in this section), we create a two-layer model within the 176 nm film: ∼45 nm of Al on a 97-nm-thick layer with unknown local thermal conductivity on a 79-nm-thick layer with known properties on diamond. Using the effective resistance data of the 79 nm film, we fit for this local conductivity and find $k_{\mathrm{Si,local}} = 16\ \mathrm{W\ m^{-1}\ K^{-1}}$ (for 79 nm $< z <$ 176 nm). We repeat this procedure for the 176 nm and 630 nm samples and fit for the local thermal conductivity characteristic of a region of 176 nm $< z <$ 630 nm. This fitted local conductivity is approximately 28 W m^{-1} K^{-1}. Because of the submicrometer thicknesses of the three films, the local conductivities and the averaged conductivities (over the entire film thickness) do not differ substantially, but the difference is expected to be significant with increasing grain size and film thickness [33].

4 Conclusions

This work investigates the thermal resistance for conduction normal to polysilicon films with three different thicknesses on a diamond substrate using TDTR and semiclassical phonon transport theory. By combining the data and the phonon transport model, we extract the cross-plane thermal conductivity of the polysilicon films (11.3 ± 3.5, 14.2 ± 3.5, and 25.6 ± 5.8 W m^{-1} K^{-1} for the 79, 176, and 630 nm films, respectively), as well as the polysilicon–diamond thermal boundary resistance (6.5–8 m^2 K GW^{-1}). The cross-plane thermal conductivity data for the 79 and 176 nm samples are consistent with simulations assuming a random grain structure with a minimum grain dimension of 50 nm and a point defect density per unit grain boundary area of $1.5 \times 10^{19}\ \mathrm{m^{-2}}$. The conductivity data for the thickest sample (630 nm) are slightly overpredicted by the random grain structure model and underpredicted by the columnar grain structure model, which indicates the transition of the grain structure from the former to the latter with increasing film thickness. Nonuniform thermal conductivity values between the samples can be attributed to the impact of spatially varying defect concentrations along the direction normal to the film.

Acknowledgment

The authors acknowledge the financial support from the Air Force Office of Scientific Research (Grant No. FA9550-12-1-0195, titled "MultiCarrier and Low-Dimensional Thermal Conduction at Interfaces for High Power Electronic Devices") and the Defense Advanced Research Projects Agency Microsystems Technology Office through the Air Force (Grant No. FA8650-10-1-7044, titled "Device-Level Thermal Management for HEMT Radar: Thermal Metrology, Interfaces, and Metrics"). The work of J. Cho was supported in part by a Samsung Scholarship.

Nomenclature

C_V = phonon specific heat per unit volume (J m^{-3} K^{-1})
d = layer thickness (m)
d_E = nondimensional layer thickness, defined in Eq. (4)
d_G = characteristic grain dimension (m)
d_{G0} = minimum grain dimension (m)
$\hbar$ = Planck's constant divided by 2π (J s)
k = thermal conductivity (W m^{-1} K^{-1})
k_B = Boltzmann's constant (J K^{-1})
$n_{GB,i}$ = number of defects of type i per unit grain boundary area (m^{-2})
R = thermal resistance (m^2 K W^{-1})
S_β = TDTR sensitivity to some parameter β
t = pump–probe delay time (s)
T = temperature (K)
v = phonon group velocity (m s^{-1})
v_s = average phonon group velocity (m s^{-1})
V_{in} = in-phase voltage of RF lock-in amplifier (V)
V_{out} = out-of-phase voltage of RF lock-in amplifier (V)
V_0 = unit volume for each atom (m^3)
x_ω = nondimensional phonon frequency = $\hbar\omega/k_B T$
z = coordinate normal to layer (m)

Greek Symbols

α = transmission coefficient
η = grain boundary scattering strength, defined by Eq. (7)
θ = Debye temperature (K)
σ_i = phonon scattering cross section of defects of type i (m^2)
τ = phonon relaxation time (s)
ω = phonon angular frequency (s^{-1})

Subscripts

b = boundary
Diam = diamond
eff = effective
GB = grain boundary
i = index denoting defect type
j = phonon branch index
L = longitudinal phonon mode
P = point defect
T = total
TO = low frequency transverse phonon mode
TU = high frequency transverse phonon mode

References

[1] Nguyen, B.-Y., Celler, G., and Mazuré, C., 2009, "A Review of SOI Technology and Its Applications," J. Integr. Circuit Syst., **4**(2), pp. 51–54.
[2] Marconnet, A. M., Asheghi, M., and Goodson, K. E., 2013, "From the Casimir Limit to Phononic Crystals: 20 Years of Phonon Transport Studies Using Silicon-on-Insulator Technology," ASME J. Heat Transfer, **135**(6), p. 061601.
[3] Hopkins, P. E., Reinke, C. M., Su, M. F., Olsson, R. H., Shaner, E. A., Leseman, Z. C., Serrano, J. R., Phinney, L. M., and El-Kady, I., 2010, "Reduction in the Thermal Conductivity of Single Crystalline Silicon by Phononic Crystal Patterning," Nano Lett., **11**(1), pp. 107–112.
[4] McConnell, A. D., and Goodson, K. E., 2005, "Thermal Conduction in Silicon Micro- and Nanostructures," Ann. Rev. Heat Transfer, **14**, pp. 129–168.
[5] Cho, J., Li, Z., Asheghi, M., and Goodson, K. E., 2014, "Near-Junction Thermal Management: Thermal Conduction in Gallium Nitride Composite Substrates," Ann. Rev. Heat Transfer (in press).
[6] Asheghi, M., Leung, Y. K., Wong, S. S., and Goodson, K. E., 1997, "Phonon-Boundary Scattering in Thin Silicon Layers," Appl. Phys. Lett., **71**(13), pp. 1798–1800.
[7] Ju, Y. S., and Goodson, K. E., 1999, "Phonon Scattering in Silicon Films With Thickness of Order 100 nm," Appl. Phys. Lett., **74**(20), pp. 3005–3007.
[8] Liu, W., and Asheghi, M., 2006, "Thermal Conductivity Measurements of Ultra-Thin Single Crystal Silicon Layers," ASME J. Heat Transfer, **128**(1), pp. 75–83.
[9] Hao, Z., Zhichao, L., Lilin, T., Zhimin, T., Litian, L., and Zhijian, L., 2006, "Thermal Conductivity Measurements of Ultra-Thin Single Crystal Silicon Films Using Improved Structure," 8th International Conference on Solid-State and Integrated Circuit Technology (ICSICT'06), Shanghai, Oct. 23–26, pp. 2196–2198.
[10] Aubain, M. S., and Bandaru, P. R., 2011, "In-Plane Thermal Conductivity Determination Through Thermoreflectance Analysis and Measurements," J. Appl. Phys., **110**(8), p. 084313.
[11] Ferrando-Villalba, P., Lopeandia, A. F., Abad, L., Llobet, J., Molina-Ruiz, M., Garcia, G., Gerbolès, M., Alvarez, F. X., Goñi, A. R., Muñoz-Pascual, F. J., and Rodríguez-Viejo, J., 2014, "In-Plane Thermal Conductivity of Sub-20 nm Thick Suspended Mono-Crystalline Si Layers," Nanotechnology, **25**(18), p. 185402.
[12] Cuffe, J., Eliason, J. K., Maznev, A. A., Collins, K. C., Johnson, J. A., Shchepetov, A., Prunnila, M., Ahopelto, J., Torres, C. S., Chen, G., and Nelson, K. A.,

Downloaded From: http://heattransfer.asmedigitalcollection.asme.org/ on 03/24/2015 Terms of Use: http://asme.org/terms

2014, "Reconstructing Phonon Mean Free Path Contributions to Thermal Conductivity Using Nanoscale Membranes," preprint arXiv:1408.6747.
[13] Chávez-Ángel, E., Reparaz, J. S., Gomis-Bresco, J., Wagner, M. R., Cuffe, J., Graczykowski, B., Shchepetov, A., Jiang, H., Prunnila, M., Ahopelto, J., Alzina, F., and Torres, C. S., 2014, "Reduction of the Thermal Conductivity in Free-Standing Silicon Nano-Membranes Investigated by Non-Invasive Raman Thermometry," APL Mater., **2**(1), p. 012113.
[14] McConnell, A. D., Uma, S., and Goodson, K. E., 2001, "Thermal Conductivity of Doped Polysilicon Layers," J. Microelectromech. Syst., **10**(3), pp. 360–369.
[15] Uma, S., McConnell, A. D., Asheghi, M., Kurabayashi, K., and Goodson, K. E., 2001, "Temperature Dependent Thermal Conductivity of Undoped Polycrystalline Silicon Layers," Int. J. Thermophys., **22**(2), pp. 605–616.
[16] Asheghi, M., Kurabayashi, K., Kasnavi, R., and Goodson, K. E., 2002, "Thermal Conduction in Doped Single-Crystal Silicon Films," J. Appl. Phys., **91**(8), pp. 5079–5088.
[17] Huxtable, S. T., Cahill, D. G., and Phinney, L. M., 2004, "Thermal Contact Conductance of Adhered Microcantilevers," J. Appl. Phys., **95**(4), pp. 2102–2108.
[18] Mandurah, M. M., Saraswat, K. C., Helms, C. R., and Kamins, T. I., 1980, "Dopant Segregation in Polycrystalline Silicon," J. Appl. Phys., **51**(11), pp. 5755–5763.
[19] ASTM, 2004, "Standard e112: Standard Test Methods for Determining Average Grain Size," ASTM International, West Conshohocken, PA.
[20] Capinski, W. S., and Maris, H. J., 1996, "Improved Apparatus for Picosecond Pump-and-Probe Optical Measurements," Rev. Sci. Instrum., **67**(8), pp. 2720–2726.
[21] Cahill, D. G., 2004, "Analysis of Heat Flow in Layered Structures for Time-Domain Thermoreflectance," Rev. Sci. Instrum., **75**(12), pp. 5119–5122.
[22] Lyeo, H.-K., and Cahill, D. G., 2006, "Thermal Conductance of Interfaces Between Highly Dissimilar Materials," Phys. Rev. B, **73**(14), p. 144301.
[23] Schmidt, A. J., Chen, X., and Chen, G., 2008, "Pulse Accumulation, Radial Heat Conduction, and Anisotropic Thermal Conductivity in Pump-Probe Transient Thermoreflectance," Rev. Sci. Instrum., **79**(11), p. 114902.
[24] Koh, Y. K., Singer, S. L., Kim, W., Zide, J. M. O., Lu, H., Cahill, D. G., Majumdar, A., and Gossard, A. C., 2009, "Comparison of the 3ω Method and Time-Domain Thermoreflectance for Measurements of the Cross-Plane Thermal Conductivity of Epitaxial Semiconductors," J. Appl. Phys., **105**(5), p. 054303.
[25] Panzer, M. A., 2010, "Thermal Characterization and Modeling of Nanostructured Materials," Ph.D. thesis, Stanford University, Stanford, CA.
[26] Cho, J., Li, Y., Hoke, W., Altman, D. H., Asheghi, M., and Goodson, K. E., 2014, "Phonon Scattering in Strained Transition Layers for GaN Heteroepitaxy," Phys. Rev. B, **89**(11), p. 115301.
[27] Cahill, D. G., Braun, P. V., Chen, G., Clarke, D. R., Fan, S., Goodson, K. E., Keblinski, P., King, W. P., Mahan, G. D., Majumdar, A., Maris, H. J., Phillpot, S. R., Pop, E., and Shi, L., 2014, "Nanoscale Thermal Transport. II. 2003–2012," Appl. Phys. Rev., **1**(1), p. 011305.
[28] Cahill, D. G., 1990, "Thermal Conductivity Measurement from 30 to 750 K: The 3ω Method," Rev. Sci. Instrum., **61**(2), pp. 802–808.
[29] Ho, C. Y., Powell, R. W., and Liley, P. E., 1972, "Thermal Conductivity of the Elements," J. Phys. Chem. Ref. Data, **1**(2), pp. 279–421.
[30] Giauque, W. F., and Meads, P. F., 1941, "The Heat Capacities and Entropies of Aluminum and Copper From 15 to 300 K," J. Am. Chem. Soc., **63**(7), pp. 1897–1901.
[31] Flubacher, P., Leadbetter, A. J., and Morrison, J. A., 1959, "Heat Capacity of Pure Silicon and Germanium and Properties of Their Vibrational Frequency Spectra," Philos. Mag., **4**(39), pp. 273–294.
[32] Graebner, J. E., 1996, "Measurements of Specific Heat and Mass Density in CVD Diamond," Diam. Relat. Mater., **5**(11), pp. 1366–1370.
[33] Graebner, J. E., Jin, S., Kammlott, G. W., Herb, J. A., and Gardinier, C. F., 1992, "Large Anisotropic Thermal Conductivity in Synthetic Diamond Films," Nature, **359**, pp. 401–403.
[34] Wort, C. J. H., Sweeney, C. G., Cooper, M. A., Scarsbrook, G. A., and Sussmann, R. S., 1994, "Thermal Properties of Bulk Polycrystalline CVD Diamond," Diam. Relat. Mater., **3**(9), pp. 1158–1167.
[35] Lee, S.-M., and Cahill, D. G., 1997, "Heat Transport in Thin Dielectric Films," J. Appl. Phys., **81**(6), pp. 2590–2595.
[36] Zeng, T., and Chen, G., 2001, "Phonon Heat Conduction in Thin Films: Impacts of Thermal Boundary Resistance and Internal Heat Generation," ASME J. Heat Transfer, **123**(2), pp. 340–347.
[37] Cahill, D. G., Goodson, K. E., and Majumdar, A., 2002, "Thermometry and Thermal Transport in Micro/Nanoscale Solid-State Devices and Structures," ASME J. Heat Transfer, **124**(2), pp. 223–241.
[38] Sood, A., Cho, J., Hobart, K. D., Feygelson, T., Pate, B., Asheghi, M., and Goodson, K. E., 2014, "Anisotropic and Nonhomogeneous Thermal Conduction in 1 μm Thick CVD Diamond," 2014 IEEE Intersociety Conference on Thermal and Thermomechanical Phenomena in Electronic Systems (ITHERM), Orlando, FL, pp. 1192–1198.
[39] Hopkins, P. E., Phinney, L. M., Serrano, J. R., and Beechem, T. E., 2010, "Effects of Surface Roughness and Oxide Layer on the Thermal Boundary Conductance at Aluminum/Silicon Interfaces," Phys. Rev. B, **82**(8), p. 085307.
[40] Gorham, C. S., Hattar, K., Cheaito, R., Duda, J. C., Gaskins, J. T., Beechem, T. E., Ihlefeld, J. F., Biedermann, L. B., Piekos, E. S., Medlin, D. L., and Hopkins, P. E., 2014, "Ion Irradiation of The Native Oxide/Silicon Surface Increases the Thermal Boundary Conductance Across Aluminum/Silicon Interfaces," Phys. Rev. B, **90**(2), p. 024301.
[41] Hopkins, P. E., Duda, J. C., Petz, C. W., and Floro, J. A., 2011, "Controlling Thermal Conductance Through Quantum Dot Roughening at Interfaces," Phys. Rev. B, **84**(3), p. 035438.
[42] Duda, J. C., and Hopkins, P. E., 2012, "Systematically Controlling Kapitza Conductance Via Chemical Etching," Appl. Phys. Lett., **100**(11), p. 111602.
[43] Wilson, R. B., and Cahill, D. G., 2014, "Anisotropic Failure of Fourier Theory in Time-Domain Thermoreflectance Experiments," Nat. Commun., **5**, p. 5075.
[44] Minnich, A. J., Johnson, J. A., Schmidt, A. J., Esfarjani, K., Dresselhaus, M. S., Nelson, K. A., and Chen, G., 2011, "Thermal Conductivity Spectroscopy Technique to Measure Phonon Mean Free Paths," Phys. Rev. Lett., **107**(9), p. 095901.
[45] Cho, J., Bozorg-Grayeli, E., Altman, D. H., Asheghi, M., and Goodson, K. E., 2012, "Low Thermal Resistances at GaN–SiC Interfaces for HEMT Technology," IEEE Electron Device Lett., **33**(3), pp. 378–380.
[46] Goodson, K. E., Kading, O. W., Rosler, M., and Zachai, R., 1995, "Experimental Investigation of Thermal Conduction Normal to Diamond-Silicon Boundaries," J. Appl. Phys., **77**(4), pp. 1385–1392.
[47] Touzelbaev, M. N., and Goodson, K. E., 1997, "Impact of Nucleation Density on Thermal Resistance near Diamond-Substrate Boundaries," J. Thermophys. Heat Transfer, **11**(4), pp. 506–512.
[48] Goodson, K. E., 1996, "Thermal Conduction in Nonhomogeneous CVD Diamond Layers in Electronic Microstructures," ASME J. Heat Transfer, **118**(2), pp. 279–286.
[49] Holland, M. G., 1963, "Analysis of Lattice Thermal Conductivity," Phys. Rev., **132**(6), pp. 2461–2471.
[50] Swartz, E. T., and Pohl, R. O., 1989, "Thermal Boundary Resistance," Rev. Mod. Phys., **61**(3), pp. 605–668.
[51] Bellis, L. D., Phelan, P. E., and Prasher, R. S., 2000, "Variations of Acoustic and Diffuse Mismatch Models in Predicting Thermal-Boundary Resistance," J. Thermophys. Heat Transfer, **14**(2), pp. 144–150.
[52] Majumdar, A., 1993, "Microscale Heat Conduction in Dielectric Thin Films," ASME J. Heat Transfer, **115**(7), pp. 7–16.
[53] Chen, G., and Tien, C. L., 1993, "Thermal Conductivities of Quantum Well Structures," J. Thermophys. Heat Transfer, **7**(2), pp. 311–318.
[54] Cahill, D. G., 1997, "Heat Transport in Dielectric Thin Films and at Solid-Solid Interfaces," Microscale Thermophys. Eng., **1**(2), pp. 85–109.
[55] Seager, C. H., 1985, "Grain Boundaries in Polycrystalline Silicon," Ann. Rev. Mater. Sci., **15**(1), pp. 271–302.
[56] Ju, S., Liang, X., and Xu, X., 2011, "Out-of-Plane Thermal Conductivity of Polycrystalline Silicon Nanofilm by Molecular Dynamics Simulation," J. Appl. Phys., **110**(5), p. 054318.

Downloaded From: http://heattransfer.asmedigitalcollection.asme.org/ on 03/24/2015 Terms of Use: http://asme.org/terms